The Effect of Carrier Doping and Thickness on the Electronic Structures of $La_3Ni_2O_7$ Thin Films

Haoliang Shi(史浩良)[1†], Zihao Huo(霍子豪)[1†], Guanlin Li(李冠霖)[1], Hao Ma(马浩)[1], Tian Cui(崔田)[1,2*], Daoxin Yao(姚道新)[3*], and Defang Duan(段德芳)[1*]

[1]*Key Laboratory of Material Simulation Methods & Software of Ministry of Education, State Key Laboratory of High Pressure and Superhard Materials, College of Physics, Jilin University, Changchun 130012, China*
[2]*Institute of High Pressure Physics, School of Physical Science and Technology, Ningbo University, Ningbo 315211, China*
[3]*Center for Neutron Science and Technology, Guangdong Provincial Key Laboratory of Magnetoelectric Physics and Devices, State Key Laboratory of Optoelectronic Materials and Technologies, School of Physics, Sun Yat-Sen University, Guangzhou 510275, China*

(Received 22 March 2025; accepted manuscript online 4 July 2025)

The discovery of high-temperature superconductivity in bilayer nickelate $La_3Ni_2O_7$ under high-pressure conditions has spurred extensive efforts to stabilize superconductivity at ambient pressure. Recently, the realization of superconductivity in compressively strained $La_3Ni_2O_7$ thin films grown on the $SrLaAlO_4$ substrates, with a T_c exceeding 40 K, represents a significant step toward this goal. Here, we investigate the influence of film thickness and carrier doping on the electronic structure of $La_3Ni_2O_7$ thin films, ranging from 0.5 to 3 unit cells, using first-principles calculations. For a 2 unit-cell film with an optimal doping concentration of 0.3 hole per formula unit (0.15 hole/Ni), the Ni-d_{z^2} interlayer bonding state crosses the Fermi level, resulting in the formation of γ pockets at the Fermi surface. These findings align with angle-resolved photoemission spectroscopy experimental data. Our results provide theoretical validation for the recent experimental discovery of ambient-pressure superconductivity in $La_3Ni_2O_7$ thin films and underscore the significant impact of film thickness and carrier doping on electronic property modulation.

DOI: 10.1088/0256-307X/42/8/080708 CSTR: 32039.14.0256-307X.42.8.080708

1. Introduction. Bilayer Ruddlesden–Popper (RP) bulk phase $La_3Ni_2O_7$ has been observed with a T_c of about 80 K at high pressure,[1–5] becoming the second unconventional superconductor family with T_c higher than the boiling temperature of liquid nitrogen, following the cuprates. Further structural analysis suggested that $La_3Ni_2O_7$ undergoes a structural transition from the ambient-pressure *Amam* phase to the high-pressure *Fmmm* or *I*4/*mmm* phase.[6,7] The underlying superconducting mechanism in this material has sparked extensive theoretical and experimental investigations.[8–30] Density functional theory (DFT)+U calculations have provided crucial insights into the electronic structure modifications under pressure, revealing the emergence of Ni-d_{z^2} orbitals near the Fermi level E_F. Whether these orbitals cross the Fermi level is crucial for the superconducting pairing mechanism, highlighting their pivotal role in achieving high-temperature superconductivity.[1,31] This electronic structure transformation corresponds to a pressure-driven Lifshitz transition, marking a fundamental change in the Fermi surface topology. The Hall resistivity measurement supports this mechanism, which has provided evidence of Ni-d_{z^2} orbital dynamics in superconducting state formation.[3]

Although bulk $La_3Ni_2O_7$ exhibits high-temperature superconductivity, this superconducting phase is exclusively observable under high pressures, which significantly complicates the investigation of its superconductivity mechanisms. To address this limitation, strain engineering has emerged as a promising strategy to stabilize superconductivity in $La_3Ni_2O_7$ at ambient pressure. For example, DFT calculations suggested that applying compressive strain along the c axis[31] or tensile strain along the a and b axes[32] would benefit superconductivity in bulk $La_3Ni_2O_7$. Recent experimental advancements have further validated this approach. Specifically, $La_3Ni_2O_7$, $La_{2.85}Pr_{0.15}Ni_2O_7$, and $La_2PrNi_2O_7$ thin films grown on $LaSrAlO_4$ (LSAO) substrates have demonstrated superconductivity above the McMillan limit (≈40 K) at ambient pressure.[33,45,46] This breakthrough underscores the potential of strain engineering as a viable strategy to stabilize and induce superconductivity in $La_3Ni_2O_7$ under ambient conditions.

In these thin film systems, precision ozone annealing plays a critical role in inducing superconductivity, as it reg-

†These authors contributed equally to this work.
*Corresponding authors. Email: cuitian@nbu.edu.cn; yaodaox@mail.sysu.edu.cn; duandf@jlu.edu.cn
© 2025 Chinese Physical Society and IOP Publishing Ltd. All rights, including for text and data mining, AI training, and similar technologies, are reserved.

ulates the ozone content and facilitates hole doping. Additionally, interfacial diffusion from the LSAO substrate can lead to Sr substitution of La/Pr near the interface, which may introduce moderate hole doping into the system. Experimental observations have shown that films with thicknesses ranging from one to three unit cells (UCs) exhibit tetragonal symmetry, although the possibility of orthorhombic symmetry cannot be entirely excluded.[34] Angle-resolved photoemission spectroscopy (ARPES) experiments have confirmed the emergence of γ pockets (associated with Ni-d_{z^2} orbitals) in the $La_{2.85}Pr_{0.15}Ni_2O_7$ films, which significantly reconstructs the electronic structure. Moreover, in thin film systems, interfacial effects become significant, and evidence obtained using photons with distinct probing depths shows that conduction is localized primarily at the first UC near the interface.[35] Therefore, it is necessary to systematically explore how the electronic structure of the ideal bilayer RP phase nickelate evolves with doping concentrations and film thicknesses.

In this study, we investigate the electronic structure of bilayer RP phase nickelate films with thicknesses ranging from a simple model of 0.5 to 3 UCs under varying carrier doping levels, using the DFT+U method. The results show that the Ni-d_{z^2} interlayer bonding state crosses the Fermi level in 1–3 UC-thick films at hole doping concentrations of 0.3–0.4 holes per formula unit (f.u.). Notably, for the 2 UC-thick film at an optimal doping concentration of 0.3 holes per f.u., the Ni-d_{z^2} interlayer bonding state crosses the Fermi level, resulting in the formation of γ pockets at the Fermi surface. This finding is in good agreement with ARPES experimental results. Additionally, the Fermi surface adopts a topological morphology resembling that of bulk materials under high pressure. We propose that hole doping plays a crucial role in modulating the electronic structure and creating favorable conditions for the emergence of novel electronic structures. These findings provide valuable insights for future experimental studies, underscoring that appropriate hole doping can effectively induce superconductivity in bilayer RP-phase nickelate thin films.

2. Computational Details. We performed first-principles calculations based on density-functional theory as implemented in the VASP code.[36] The exchange-correlation effects were treated within the generalized gradient approximation using the Perdew–Burke–Ernzerhof functional, and the projector augmented-wave pseudopotentials were employed with valence electron configurations of $5s^25p^65d^16s^2$ for La, $3s^23p^63d^84s^2$ for Ni, and $2s^22p^4$ for O.[37,38] In order to consider the *in situ* Coulomb repulsion effect of Ni atoms, we applied $U = 3.5$ eV on Ni atoms to simulate the static correlation effect.[39,40] A plane-wave cutoff energy of 700 eV and a k-point grid spacing of $2\pi \times 0.03$ Å^{-1} were chosen to ensure a balance between computational efficiency and energy convergence.

The crystal structures of $La_3Ni_2O_7$ thin films with thicknesses ranging from 0.5 to 3 UCs were constructed based on experimentally determined structural parameters, utilizing slices of both the tetragonal ($I4/mmm$) and orthorhombic ($Amam$) phases. For the tetragonal phase, the lattice constants were set to $a = b = 3.77$ Å, while for the orthorhombic phase, $a = 5.36$ Å and $b = 5.30$ Å were used, ensuring that the squared average of a and b matched 3.77 Å. A vacuum layer of 20 Å was introduced along the direction perpendicular to the bilayer to minimize interactions between periodic images. The lattice constants in the a and b directions were fixed, while the atomic positions were fully relaxed. To account for carrier doping effects due to interface effects, substrate Sr diffusion, and other factors, doping levels ranging from 0.2 electrons to 1 hole per f.u. were systematically investigated.

3. Results and Discussion. Using experimentally determined lattice constants, we constructed structural models of $La_3Ni_2O_7$ thin films with thicknesses ranging from 0.5 to 3 UC. Figure 1(a) illustrates the tetragonal structure of a representative 3 UC-thick film. The thickness dependence of out-of-plane Ni-O bond lengths is systematically analyzed in Fig. 1(b), with data points corresponding to both outer (o_1–o_6) and inner (i_1–i_6) sides of the bilayer. For clarity, only the first three bilayers are shown, as the remaining double layers can be determined through symmetrical operations corresponding to those already depicted. Our comprehensive analysis reveals three fundamental characteristics of the Ni-O bond length distribution: (1) The bond lengths at the inner sides (<2.1 Å) maintain shorter values than those at the outer sides (>2.1 Å), showing thickness-independent behavior. (2) Significant differences are observed between the surface bilayer (i_1 = 1.93 Å, i_2 = 2.07 Å for 3 UC) and interior bilayers (i_1–i_6 are 1.97 Å for 3 UC), indicating that

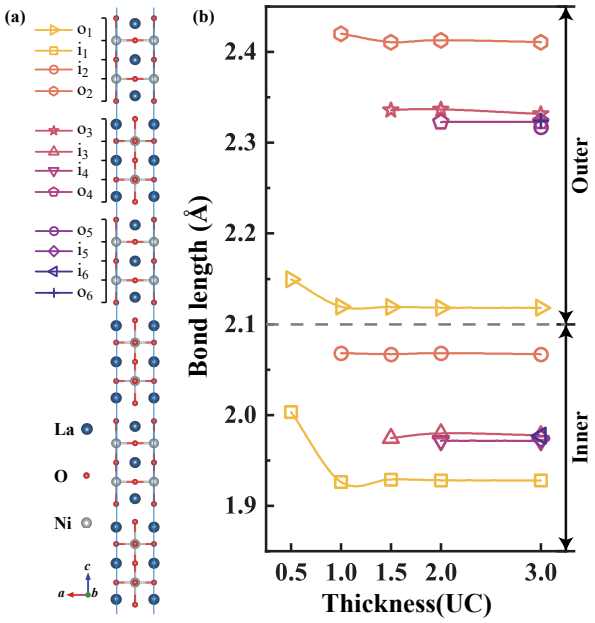

Fig. 1. The structure and geometric characteristics of tetragonal $La_3Ni_2O_7$ thin films. (a) The structure of the 3 UC-thick $La_3Ni_2O_7$ thin film, where blue, silver, and red spheres represent La, Ni, and O atoms, respectively. The labels o_1–o_6 and i_1–i_6 denote the out-of-plane Ni-O bond lengths at the outer and inner sides of the bilayer, respectively. (b) The out-of-plane Ni-O bond lengths as a function of film thickness. The color gradient from yellow to purple indicates increasing distance from the film surface.

geometric reconstruction primarily affects the surface bilayers. (3) The 0.5 UC-thick film exhibits distinct bond length characteristics compared to thicker films (>1 UC), suggesting significant structural reconstruction effects at this critical thickness. These systematic variations in geometric parameters provide strong evidence for surface reconstruction in the outermost layers of $La_3Ni_2O_7$ thin films. The reconstructed surface structure, characterized by modified Ni-O bond lengths, may lead to distinct electronic properties compared to those of the bulk compound.

We then calculated the Ni-d_{z^2} density of states (DOS) at the Fermi level as a function of carrier doping concentration for films with varying thicknesses, as shown in Fig. 2. The carrier doping concentration was varied from 0.2 electrons to 1.0 hole per f.u., corresponding to a nominal Ni valence state ranging from 2.6 to 2.0. For the tetragonal phase with a film thickness of 0.5 UC, the Ni-d_{z^2} DOS reaches its maximum value in the undoped case, as shown in Fig. 2(a). However, both electron and hole doping lead to a reduction in the Ni-d_{z^2} DOS at the Fermi level as the doping concentration increases. This suggests that carrier doping in the 0.5 UC-thick film model may not be favorable for enhancing superconductivity. In the case of a 1 UC-thick film, the Ni-d_{z^2} DOS slightly increases as the electron doping concentration increases from 0 to 0.2 electrons/f.u., indicating that electron doping has a negligible effect on the Ni-d_{z^2} DOS. For hole doping, the Ni-d_{z^2} DOS at the Fermi level remains relatively constant at low doping concentrations; however, a significant increase to 1.5 states·eV^{-1}·f.u.$^{-1}$ is observed at a doping concentration of 0.4 holes/f.u. (0.2 hole/Ni). As the hole doping concentration further increases, the Ni-d_{z^2} DOS reaches a maximum value of 3.05 states·eV^{-1}·f.u.$^{-1}$ at 0.6 holes/f.u., followed by a subsequent decrease. For film thicknesses of 1.5–3 UC, the relationship between the Ni-d_{z^2} DOS and doping concentration follows a similar trend compared to that of the 1 UC-thick film case. The maximum Ni-d_{z^2} DOS values for these thicknesses also occur at a doping concentration of 0.6 hole/f.u., with 1.99 states·eV^{-1}·f.u.$^{-1}$ for 1.5 UC-thick film, 2.28 states·eV^{-1}·f.u.$^{-1}$ for 2 UC-thick film, 2.26 states·eV^{-1}·f.u.$^{-1}$ for 3 UC-thick film. These results highlight the consistent behavior of the Ni-d_{z^2} DOS across 1–3 UC thicknesses under hole doping conditions.

For the orthorhombic phase, the Ni-d_{z^2} DOS exhibits similar variations to those of the tetragonal phase with doping concentration and film thickness, as shown in Fig. 2(b). For the 0.5 UC-thick film, the Ni-d_{z^2} DOS has a value of 0.75 states·eV^{-1}·f.u.$^{-1}$ for the undoped case. Upon doping, the DOS peaks at 0.85 states·eV^{-1}·f.u.$^{-1}$ with 0.2 electrons/f.u., and significantly increases to 1.73 states·eV^{-1}·f.u.$^{-1}$ with 0.6 holes/f.u. In the case of a 1 UC-thick film, when the doping concentration of electrons rises from 0 to 0.2 electrons/f.u., the Ni-d_{z^2} DOS demonstrates a moderate increase from 0.32 to 0.68 states·eV^{-1}·f.u.$^{-1}$, indicating a relatively weak influence of electron doping. Conversely, hole doping induces a more pronounced effect, with the Ni-d_{z^2} DOS reaching a maximum value of 2.41 states·eV^{-1}·f.u.$^{-1}$

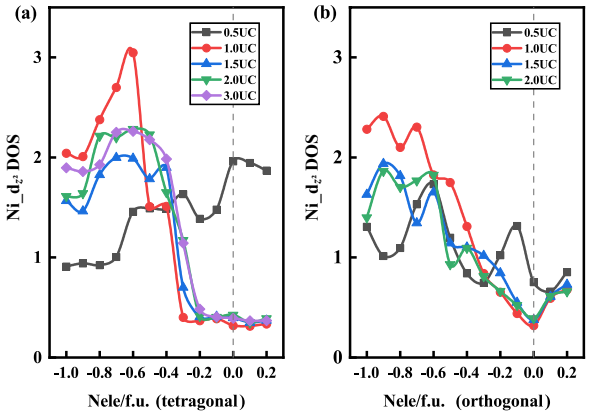

Fig. 2. The density of states of Ni-d_{z^2} at the Fermi level as a function of carrier doping concentration (NE, number of electrons) for (a) tetragonal and (b) orthorhombic symmetry. Black square, red circle, blue upward triangle, green downward triangle, and purple diamond represent 0.5, 1.0, 1.5, 2.0, and 3.0 UC-thick film thicknesses, respectively.

at 0.9 holes/f.u., followed by a subsequent decrease. This trend persists in the films with thicknesses ranging from 1.5 to 3 UC thick, where the Ni-d_{z^2} DOS similarly peaks at 0.9 holes/f.u., with maximum values of 1.943 states·eV^{-1}·f.u.$^{-1}$ for 1.5 UC-thick film model and 1.86 states·eV^{-1}·f.u.$^{-1}$ for 2 UC-thick film model.

According to previous studies, the Fermi surface of bulk $La_3Ni_2O_7$ under high pressure exhibits three Fermi sheets:[13] the α and β pockets dominated by the Ni-$d_{x^2-y^2}$ orbitals, while the γ pocket, dominated by the Ni-d_{z^2} orbital, emerges near the M points and is proposed to play a critical role in superconductivity. In the thin-film system, environmental asymmetry induces significant changes in the Fermi surface properties.

For the 0.5 UC-thick film, the γ pocket persists even in the undoped case [see Fig. 3(a)], likely due to pronounced surface reconstruction. However, when compared with ARPES experimental measurements of the Fermi surface, we observe that the α and β pockets in the 0.5 UC model do not align with the experimentally observed Fermi pockets.

For the 1 UC film, the α and β pockets exhibit pronounced separation along the Γ–M direction, as shown in Fig. 3(b). Layer-resolved partial charge density projections of Ni-$d_{x^2-y^2}$ bands along the Γ–M direction (Fig. S39 of the Supplementary Materials (SM)] reveal a distinct energetic splitting: surface-localized states occupy lower energies, while inner-layer states dominate at higher energies. This splitting is maximized in the 1 UC film due to the strong contrast between its surface-proximal layer and the adjacent inner layer. Notably, in the 1 UC-thick thin film, the Ni-d_{z^2} orbital does not cross the Fermi level at this doping concentration. It crosses the Fermi level only under a slightly higher hole-doping condition of 0.4 holes/f.u.

For the 2 UC-thick film, we systematically calculated its electronic structure under different doping conditions, as shown in Fig. S1–S26 of the SM. We found that doping with 0.3 holes/f.u. could cause a Lifshitz transition, leading to the formation of a hole-type Fermi pocket around

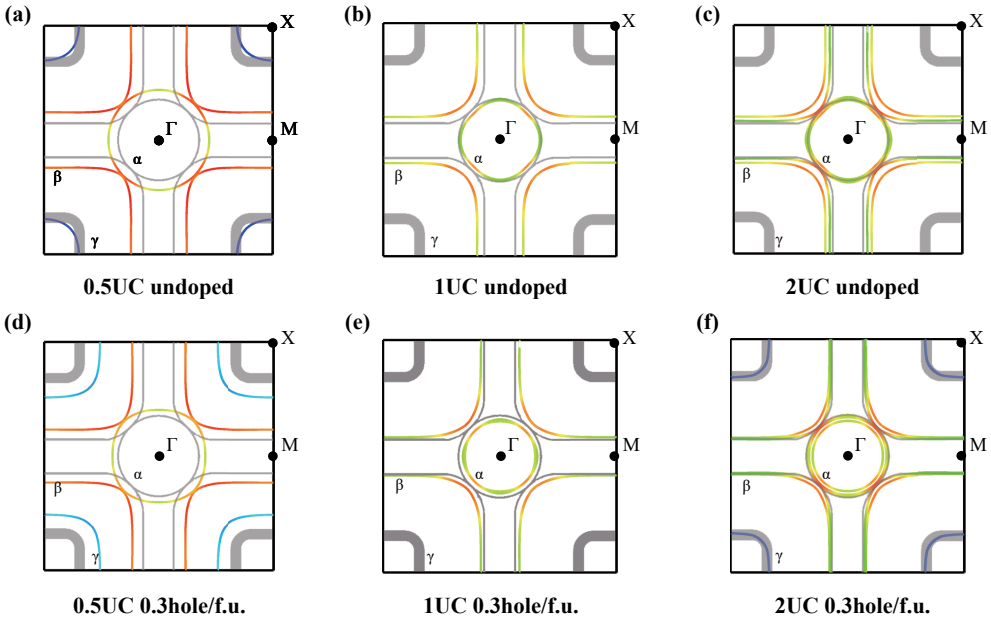

Fig. 3. Fermi surface of the tetragonal phase with different thicknesses and doping concentrations. The colors projected onto the Fermi surface represent the Fermi velocity. (a) A 0.5 UC-thick film without doping. (b) A 1 UC-thick film without doping. (c) A 2 UC-thick film without doping. (d) A 0.5 UC-thick film with 0.3 holes/f.u. (e) A 1 UC-thick film with 0.3 holes/f.u. (f) A 2 UC-thick film with 0.3 holes/f.u.

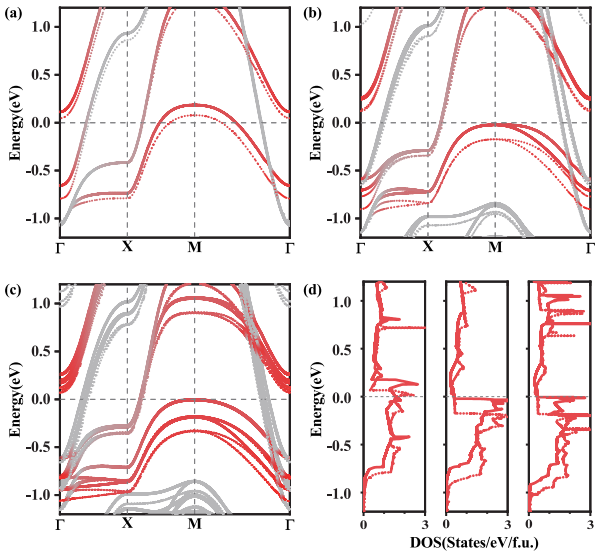

Fig. 4. Electronic properties of the tetragonal phase with different thicknesses [(a) 0.5 UC, (b) 1 UC, and (c) 2 UC] and doping concentrations. The solid line represents the band structure doped with 0.3 holes/f.u., while the dashed line represents the band structure under undoped conditions. The red coloration projected onto the band structure represents the projection of the Ni-d_{z^2} orbital. (d) The Ni-d_{z^2} orbital projected density states of 0.5, 1, and 2 UC-thick films correspond to the (a), (b), and (c) panels, respectively.

the M point on the Fermi surface. This transition corresponds to the upward shift of the Ni-d_{z^2} energy band [see the solid line bands in Fig. 4(c)]. Notably, the resulting γ pocket is significantly larger compared to that of the bulk structure at 20 GPa. Furthermore, the Fermi surface of the 2 UC-thick film doped with 0.3 holes/f.u. (0.15 holes/Ni) [Fig. 3(f)] is in good agreement with ARPES measurements,[35] sharing comparable sizes and topological features. Our findings highlight the critical interplay between film thickness and doping concentration in tuning electronic properties of $La_3Ni_2O_7$ thin films, offering valuable insights for optimizing their electronic characteristics in potential experimental studies and novel applications. While our current DFT+U approach successfully captures thickness- and doping-dependent electronic structures, we recognize that a more comprehensive theoretical framework incorporating advanced many-body techniques (such as dynamical mean-field theory or cellular dynamical mean-field theory) would be valuable for fully elucidating the complex interplay of electronic correlations in this system—an important direction for future theoretical investigations.

Since the case of 0.3 holes/f.u. doping aligns most closely with ARPES experimental results, we compared the electronic structures with varying thicknesses under both undoped and 0.3 hole-doped conditions. As hole doping is introduced, the increased onsite energy of the Ni-d_{z^2} orbital induces a significant upward shift of its associated bands, as shown in Fig. 4. For the 0.5 UC-thick film, the introduction of hole doping causes the Ni-d_{z^2} bonding band to move away from the Fermi level, resulting in a downward shift of the projected DOS of the Ni-d_{z^2} orbital. For the 1 UC-thick film, a doping concentration of 0.3 holes/f.u. shifts the Ni-d_{z^2} bonding band closer to but not across the Fermi level. For the 2 UC-thick film, this same doping concentration causes the Ni-d_{z^2} bonding band to move closer to and make contact with the Fermi level at the M point. This electronic structure transformation corresponds to a Lifshitz transition, marking a fundamental change in Fermi surface topology. This feature is crucial for the emer-

gence of superconductivity in bulk compounds under high pressure.[13,20,25,41] Moreover, for a 2 UC-thick film, the Ni-d_{z^2} DOS at Fermi level is 2.20 states·eV^{-1}·f.u.$^{-1}$, which is comparable to that of bulk $I4/mmm$ phase at 30 GPa (2.2 states·eV^{-1}·f.u.$^{-1}$).[31] The high DOS at E_F combined with presence of hole pockets provides a theoretical explanation for experimentally observed superconductivity in thin films. Furthermore, the Ni-d_{z^2} bonding energy band of the 2 UC-thick thin film splits at the M point, with higher-energy band forming the hole pocket. We suspect that this is due to non-equivalent bilayers contributing their Ni-d_{z^2} orbitals to different energy bands.

To elucidate the origin of the higher-energy band, we conducted atomically resolved orbital-projection analyses to identify the specific Ni atomic layer responsible for the higher-energy orbital. The projected band structure demonstrates that Ni atoms within the surface-proximal bilayer (adjacent to the vacuum layer) exhibit higher-energy states and predominantly contribute to the Fermi-level-crossing band, as shown in Fig. 5. This implies that superconductivity likely emerges preferentially in the interfacial bilayer. When considered alongside geometric reconstruction and Sr interdiffusion effects, these orbital-projected results further highlight the critical influence of interfacial configurations on superconducting properties.

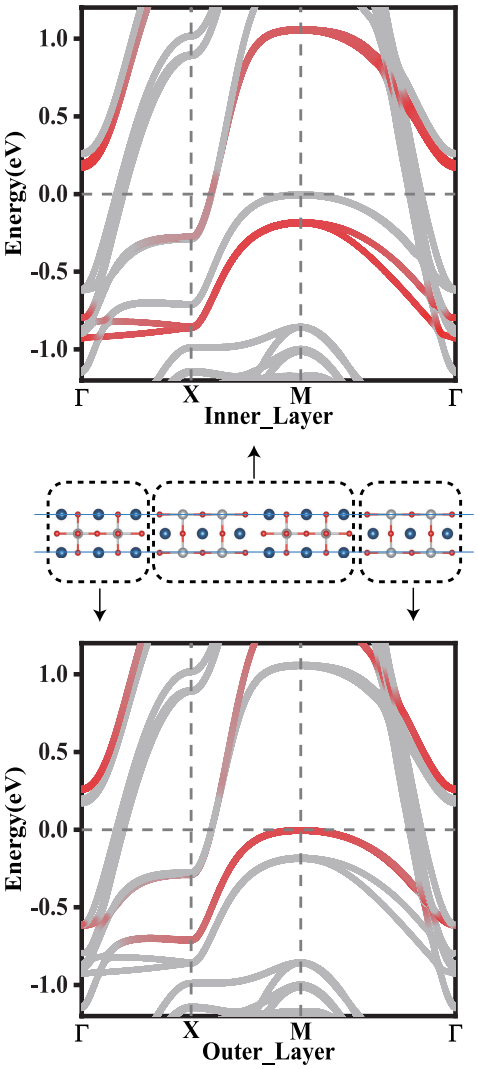

Fig. 5. The projected band structure of the 2 UC-thick tetragonal phase thin film doped with 0.3 holes/f.u. The upper and lower figures project the Ni-d_{z^2} orbitals (red) onto the bilayer of the outer and inner sides, respectively.

In realistic experimental scenarios, hole doping can arise from Sr inter-diffusion from the substrate into the $La_3Ni_2O_7$ lattice, while electron doping may originate from oxygen vacancy formation within the $La_3Ni_2O_7$ itself. Therefore, we conducted additional calculations to simulate experimentally viable doping mechanisms, including Sr doping and oxygen vacancies. For hole doping, we modeled Sr substitutions [$La_{(1-x)}Sr_xNi_2O_7$, $0.1 \leqslant x \leqslant 1$] using the virtual crystal approximation and calculated their band structures, as shown in Figs. S27–S36 of the SM. Notably, for Sr doping of La:Sr = 7:3–6:4 (0.3–0.4 holes/f.u.), the Ni-d_{z^2} orbital-derived band crosses the Fermi level, a behavior closely aligned with the 0.3 holes/f.u. critical doping level identified in our preceding analysis. For electron doping, we explicitly modeled oxygen vacancies ($La_3Ni_2O_{7-\delta}$, δ = 0.125–0.25) by constructing a $\sqrt{2} \times \sqrt{2} \times 1$ supercell with apical oxygen removed, as shown in Figs. S37 and S38. Our calculations reveal a thermodynamic preference for vacancies in the inner bilayer, with total energy differences of 30 meV/f.u. (single vacancy) and 58 meV/f.u. (double vacancies) compared to outer-layer vacancies. Furthermore, we show the energy distance of the Ni-d_{z^2}-dominated flat band from the Fermi surface as a function of doping concentration via different models (see Fig. 6). In the hole-doping regime, the Ni-d_{z^2} energies obtained through total electron count adjustment show excellent agreement with Sr substitution. In the electron-doping regime, it aligns with inner-layer oxygen vacancy doping, the thermodynamically preferred vacancy configuration. This consistency confirms the effectiveness of our carrier doping methodology in accurately modeling both hole and electron doping scenarios.

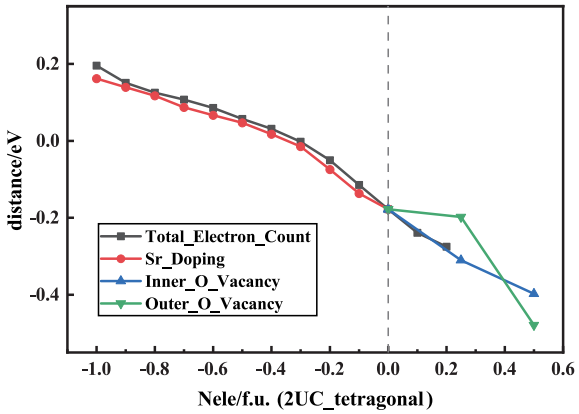

Fig. 6. The energy distance of the Ni-d_{z^2}-dominated flat band from the Fermi surface modulated by different doping concentrations as a function of carrier doping via different models: black squares (carrier doping), red circles (virtual crystal approximation-simulated Sr doping), blue triangles (inner-bilayer oxygen vacancies), and green triangles (outer-bilayer oxygen vacancies).

4. Conclusions. In summary, we have performed a comprehensive first-principles study to investigate the effects of film thickness and carrier doping on the electronic structure of $La_3Ni_2O_7$ thin films with thicknesses ranging from 0.5 to 3 UC. Our results show that the 1–3 UC-thick films with optimal doping levels lead to an upward shift of the Ni-d_{z^2} bands and the formation of γ pockets at the Fermi surface. Notably, the 2 UC film doped with 0.3 holes/f.u. matches those observed in ARPES experiments, and the conductivity primarily originates from the interfacial layer. The results underline the importance of hole doping in achieving optimal superconducting properties. Our work provides a robust theoretical framework that aligns with recent experimental observations of ambient-pressure superconductivity in $La_3Ni_2O_7$ thin films. This work underscores the significance of carrier doping and paves the way for future experimental and theoretical investigations.

Note Added. Upon completion of this work, we noted several independent studies exploring superconductivity in $La_3Ni_2O_7$ thin films, each employing distinct methodologies and focusing on different aspects of the material's properties.[42–44] In comparison, our study provides a systematic exploration of the interplay between carrier doping and film thickness in $La_3Ni_2O_7$ thin films. This approach underscores the significance of doping effects and optimal thickness in stabilizing superconducting states, offering a broader perspective on the factors governing superconductivity in this system and complementing the existing literature.

Acknowledgements. We thank Prof. Zhuoyu Chen and Prof. Yuefeng Nie for the experimental data and discussion and thank Prof. Weiqiang Chen for many stimulating discussions. This work was supported by the National Key R&D Program of China (Gran Nos. 2022YFA1402304 and 2022YFA1402802), the National Natural Science Foundation of China (Grant Nos. 12494591, 12122405, 12274169, and 92165204), Program for Science and Technology Innovation Team in Zhejiang (Grant No. 2021R01004), Guangdong Provincial Key Laboratory of Magnetoelectric Physics and Devices (Grant No. 2022B1212010008), Guangdong Fundamental Research Center for Magnetoelectric Physics (2024B0303390001), Guangdong Provincial Quantum Science Strategic Initiative (Grant No. GDZX2401010), and the Fundamental Research Funds for the Central Universities. Some of the calculations were performed at the High Performance Computing Center of Jilin University and using TianHe-1(A) at the National Supercomputer Center in Tianjin.

References

[1] Sun H, Huo M, Hu X, Li J, Liu Z, Han Y, Tang L, Mao Z, Yang P, Wang B, Cheng J, Yao D X, Zhang G M, and Wang M 2023 *Nature* **621** 493
[2] Hou J, Yang P, Liu Z, Li J, Shan P, Ma L, Wang G, Wang N, Guo H, Sun J, Uwatoko Y, Wang M, Zhang G, Wang B, and Cheng J 2023 *Chin. Phys. Lett.* **40** 117302
[3] Zhang Y, Su D, Huang Y, Shan Z, Sun H, Huo M, Ye K, Zhang J, Yang Z, Xu Y, Su Y, Li R, Smidman M, Wang M, Jiao L, and Yuan H 2024 *Nat. Phys.* **20** 1269
[4] Zhou Y, Guo J, Cai S, Sun H, Wang P, Zhao J, Han J, Chen X, Wu Q, Ding Y, Wang M, Xiang T, Mao H, and Sun L 2023 arXiv:2311.12361 [cond-mat.supr-con]
[5] Wang G, Wang N N, Shen X L, Hou J, Ma L, Shi L F, Ren Z A, Gu Y D, Ma H M, Yang P T, Liu Z Y, Guo H Z, Sun J P, Zhang G M, Calder S, Yan J Q, Wang B S, Uwatoko Y, and Cheng J G 2024 *Phys. Rev. X* **14** 011040
[6] Wang L, Li Y, Xie S Y, Liu F, Sun H, Huang C, Gao Y, Nakagawa T, Fu B, Dong B, Cao Z, Yu R, Kawaguchi S I, Kadobayashi H, Wang M, Jin C, Mao H K, and Liu H 2024 *J. Am. Chem. Soc.* **146** 7506
[7] Li J, Ma P, Zhang H, Huang X, Huang C, Huo M, Hu D, Dong Z, He C, Liao J, Chen X, Xie T, Sun H, and Wang M 2024 arXiv:2404.11369 [cond-mat.supr-con]
[8] Luo Z, Hu X, Wang M, Wú W, and Yao D X 2023 *Phys. Rev. Lett.* **131** 126001
[9] Gu Y, Le C, Yang Z, Wu X, and Hu J 2023 arXiv:2306.07275 [cond-mat.supr-con]
[10] Yang Q G, Wang D, and Wang Q H 2023 *Phys. Rev. B* **108** L140505
[11] Shilenko D A and Leonov I V 2023 *Phys. Rev. B* **108** 125105
[12] Chen X, Jiang P, Li J, Zhong Z, and Lu Y 2023 arXiv:2307.07154 [cond-mat.supr-con]
[13] Liu Y B, Mei J W, Ye F, Chen W Q, and Yang F 2023 *Phys. Rev. Lett.* **131** 236002
[14] Christiansson V, Petocchi F, and Werner P 2023 *Phys. Rev. Lett.* **131** 206501
[15] Zhang Y, Lin L F, Moreo A, and Dagotto E 2023 *Phys. Rev. B* **108** L180510
[16] Liao Z, Chen L, Duan G, Wang Y, Liu C, Yu R, and Si Q 2023 *Phys. Rev. B* **108** 214522
[17] Lechermann F, Gondolf J, Bötzel S, and Eremin I M 2023 *Phys. Rev. B* **108** L201121
[18] Shen Y, Qin M, and Zhang G M 2023 *Chin. Phys. Lett.* **40** 127401
[19] Yang Y F, Zhang G M, and Zhang F C 2023 *Phys. Rev. B* **108** L201108
[20] Huang J, Wang Z D, and Zhou T 2023 *Phys. Rev. B* **108** 174501
[21] Qin Q and Yang Y f 2023 *Phys. Rev. B* **108** L140504
[22] Luo Z, Lv B, Wang M, Wu W, and Yao D 2023 arXiv:2308.16564 [cond-mat.supr-con]
[23] Lu C, Pan Z, Yang F, and Wu C 2024 *Phys. Rev. Lett.* **132** 146002
[24] Zhang Y, Lin L F, Moreo A, Maier T A, and Dagotto E 2024 *Nat. Commun.* **15** 2470
[25] Wú W, Luo Z, Yao D X, and Wang M 2024 *Sci. China-Phys. Mech. Astron.* **67** 117402
[26] Sakakibara H, Kitamine N, Ochi M, and Kuroki K 2024 *Phys. Rev. Lett.* **132** 106002
[27] Qu X Z, Qu D W, Chen J, Wu C, Yang F, Li W, and Su G 2024 *Phys. Rev. Lett.* **132** 036502
[28] Jiang K, Wang Z, and Zhang F C 2024 *Chin. Phys. Lett.* **41** 017402
[29] Cao Y and Yang Y f 2024 *Phys. Rev. B* **109** L081105
[30] Tian Y H, Chen Y, Wang J M, He R Q, and Lu Z Y 2024 *Phys. Rev. B* **109** 165154
[31] Huo Z H, Luo Z H, Zhang P, Yang A Q, Liu Z T, Tao X R, Zhang Z H, Guo S M, Jiang Q W, Chen W X, Yao D X, Duan D F, and Cui T 2025 *Sci. China-Phys. Mech. Astron.* **68** 237411
[32] Geisler B, Hamlin J J, Stewart G R, Hennig R G, and Hirschfeld P J 2024 arXiv:2411.14600 [cond-mat.supr-con]
[33] Ko E K, Yu Y, Liu Y, Bhatt L, Li J, Thampy V, Kuo C T, Wang B Y, Lee Y, Lee K, Lee J S, Goodge B H, Muller D A, and Hwang H Y 2024 *Nature* **638** 935

[34] Bhatt L, Jiang A Y, Ko E K, Schnitzer N, Pan G A, Šegedin D, Liu Y, Yu Y, Zhao Y F, Morales E A, Brooks C M, Botana A S, Hwang H Y, Mundy J A, Muller D A, and Goodge B H 2025 arXiv:2501.08204 [cond-mat.supr-con]

[35] Li P, Zhou G, Lv W, Li Y, Yue C, Huang H, Xu L, Shen J, Miao Y, Song W, Nie Z, Chen Y, Wang H, Chen W, Huang Y, Chen Z H, Qian T, Lin J, He J, Sun Y, Chen Z, and Xue Q K 2025 arXiv:2501.09255 [cond-mat.supr-con]

[36] Kresse G and Furthmüller J 1996 *Comput. Mater. Sci.* **6** 15

[37] Blöchl P E 1994 *Phys. Rev. B* **50** 17953

[38] Perdew J P, Burke K, and Ernzerhof M 1996 *Phys. Rev. Lett.* **77** 3865

[39] Dudarev S L, Botton G A, Savrasov S Y, Humphreys C J, and Sutton A P 1998 *Phys. Rev. B* **57** 1505

[40] Liechtenstein A I, Anisimov V I, and Zaanen J 1995 *Phys. Rev. B* **52** R5467

[41] Oh H and Zhang Y H 2023 *Phys. Rev. B* **108** 174511

[42] Shao Z Y, Liu Y B, Liu M, and Yang F 2025 arXiv:2501.10409 [cond-mat.supr-con]

[43] Yue C, Miao J J, Huang H, Hua Y, Li P, Li Y, Zhou G, Lv W, Yang Q, Sun H, Sun Y, Lin J, Xue Q K, Chen Z, and Chen W 2025 arXiv:2501.06875 [cond-mat.str-el]

[44] Le C, Zhan J, Wu X, and Hu J 2025 arXiv:2501.14665 [cond-mat.supr-con]

[45] Liu Y, Ko E K, Tarn Y, Bhatt L, Goodge B H, Muller D A, Raghu S, Yu Y, and Hwang H Y 2025 arXiv:2501.08022 [cond-mat.supr-con]

[46] Zhou G, Lv W, Wang H, Nie Z, Chen Y, Li Y, Huang H, Chen W, Sun Y, Xue Q K, and Chen Z 2024 arXiv:2412.16622 [cond-mat.supr-con]